Half-integer Wannier Diagram and Brown-Zak Fermions of Graphene on Hexagonal Boron-Nitride.

T. Fabian, M. Kausel, L. Linhart, J. Burgdörfer, and F. Libisch*,
Institute for Theoretical Physics, TU Wien, 1040 Vienna, Austria, EU
*Corresponding author; E-mail: florian.libisch@tuwien.ac.at. ©2022 American Physical Society.
This is the peer reviewed version of Physical Review B (Vol. 106, Issue 16). American Physical Society (APS), which has been published in final form at https://doi.org/10.1103/physrevb.106.165412.
(Dated: September 10th 2022)

The moiré potential of graphene on hexagonal boron nitride (hBN) generates a supercell sufficiently large as to thread a full magnetic flux quantum Φ_0 for experimentally accessible magnetic field strengths. Close to rational fractions of Φ_0, $p/q \cdot \Phi_0$, magnetotranslation invariance is restored giving rise to Brown-Zak fermions featuring the same dispersion relation as in the absence of the field. Employing a highly efficient numerical approach we simulate the magnetoconductance of bulk graphene on hexagonal boron nitride. The resulting Hofstadter butterfly is analyzed in terms of a novel half-integer Wannier diagram for Landau spectra of Dirac particles. This complex diagram can account for many features observed in the simulation and in experiment on a single-particle level, such as spin and valley degeneracy lifting and a non-periodicidy in Φ_0.

Ultraclean graphene in crystallographic alignment with hexagonal boron nitride (hBN) forms large-scale moiré patterns[1, 2]. The area $S \approx 165$ nm^2 of one supercell is large enough to reach the regime of one magnetic flux quantum $\Phi_0 = h/e$ per moiré unit cell already at $B = 23.5$ T. A plethora of fascinating phenomena emerge such as Hofstadter's butterfly, the fractal energy spectrum of the lattice in the magnetic field [3, 4], Weiss oscillations [5, 6] and Brown-Zak oscillations [7–9], i.e., revivals of zero-field conductivity at large magnetic fields periodic in $1/B$. Indeed, Hofstadter's butterfly could recently be experimentally observed [10–17]. For exactly rational fractions $p/q\,\Phi_0$ of the magnetic flux quantum corresponding to magnetic field values $B_{p/q} = p/q\,\Phi_0/S$, the resulting Bloch wavefunction is strictly periodic and magnetotranslational invariance is restored. Bloch's theorem predicts new quasi-particles, so-called Brown-Zak fermions (BZfs) [7–9], which travel, undeflected by the magnetic field, ballistically through the moiré superlattice [3, 4, 7–9, 15–24]. Inprints of BZfs in terms of periodic oscillations of the conductance in $1/B$ (for fixed p), the Brown-Zak oscillations, have been observed up to high temperatures [15, 16].

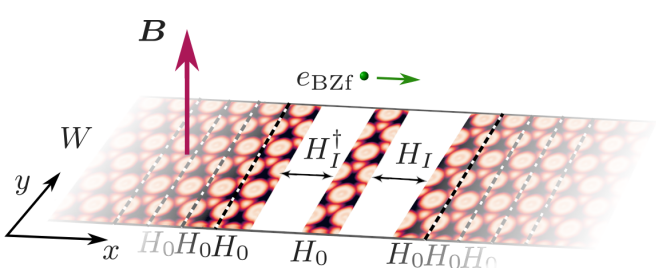

FIG. 1. Build-up of the graphene nanoribbon from periodic repetition of a single building block, schematically. A "slice" with the width of one moiré cell described by H_0 is joined by the interaction H_I with adjacent identical slices to the right and left along the propagation direction x of the Brown-Zak fermion (BZf). The width $W = 750$ nm of the nanoribbon is in y-direction. The magnetic field is oriented perpendicular to the plane of the ribbon.

Hofstadter's butterfly in graphene was previously discussed using Wannier's formula [20] originally derived for a system with parabolic dispersion. In the present work, we calculate the full Wannier diagram for graphene on hexagonal boron nitride based on an ab-initio parametrization of the supercell, including strain effects. We show that the linear dispersion of graphene leads to a modified *half-integer* Wannier equation (Eq. (6), in line with the *half-integer* quantum Hall effect in graphene. We further show that inclusion of spin- and valley degeneracy lifting provides a consistent single-particle explanation for several recent measurements[10–17].

The large supercell of graphene aligned on hexagonal boron nitride includes roughly ten thousand atoms rendering numerical simulations of the conductance challenging [25]. Calculations therefore have focused on the density of states [26–28], a continuum $k \cdot p$ Hamiltonian [24, 29], scaled graphene[30, 31], or on effective 1D models[6]. Here we simulate transport through aligned ($\Theta = 0$) graphene on hexagonal boron nitride in a large-scale tight-binding (TB) approach with the Hamiltonian

$$H = \sum_{i,j} t_{ij} c_i c_j^\dagger + \sum_i V_i c_i c_i^\dagger + g_s \mu_B \hat{S} \cdot \hat{B}, \qquad (1)$$

hoppings t_{ij}, on site-potential V_i, a Zeeman term with $g_s = 2$ and Bohr magneton μ_B without further approximations. The valley degree of freedom of graphene is implicitly contained in the full TB treatment of the lattice and the spin degree of freedom enters through the Zeeman term. We first parametrize of the atomistic moiré lattice in configuration space by a set of ab-initio DFT calculations[32] of primitive cells[33, 34]. We then use a mechanical elasticity model to account for the structural geometry relaxation and induced strain on the graphene layer by the hBN substrate [35, 36] to build an ab-initio derived graphene/hBN structure (see Appendix A). We treat a realistic 750 nm wide ribbon with zig-zag edges locally covered by a Berry-Mondragon potential to suppress edge states[37]. We incorporate a magnetic field through a Peierls substitution with gauge $\mathbf{A} = (B \cdot y, 0, 0)$ to retain translational invariance in x direction (i.e., along the ribbon).

We compute the bandstructure $E(k)$ of the ribbon for varying magnetic fields B from

$$\left(H_0 + \mathrm{e}^{\mathrm{i}k\Delta x} H_I + \mathrm{e}^{-\mathrm{i}k\Delta x} H_I^\dagger\right) \psi_n = E_n(k)\, \psi_n, \qquad (2)$$

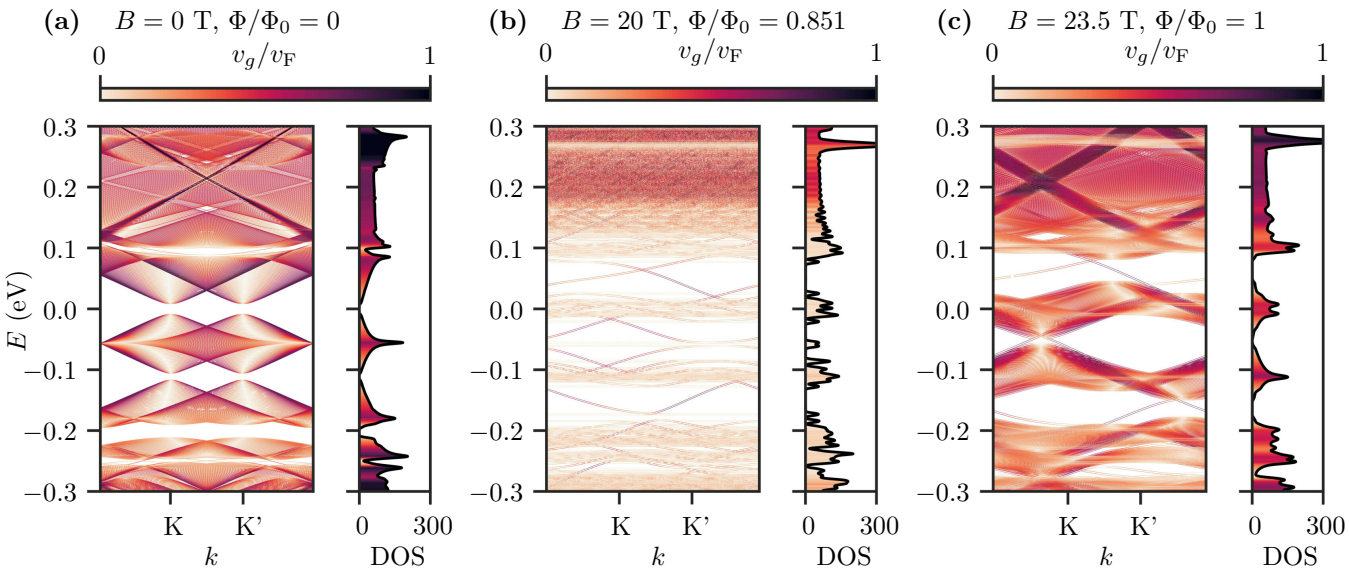

FIG. 2. Band structure and density of states (DOS) in units $n/n_0/eV$ of a 750 nm wide graphene ribbon aligned on hBN in perpendicular magnetic fields **(a)** $B = 0$ T ($\Phi/\Phi_0 = 0$), **(b)** $B = 20$ T ($\Phi/\Phi_0 = 0.851$), **(c)** $B = 23.5$ T ($\Phi/\Phi_0 = 1$). The bandstructure is shaded according to the group velocity relative to v_F, the group velocity of the massless Dirac fermions in (*a*).

where $H_0 \in \mathbb{C}^{N\times N}$ is the Hamiltonian of a "slice" of the ribbon (N is the number of sites of the ribbon unit cell) with a width in y-direction of 60 moiré unit cells containing approximately $N \approx 8\times 10^5$ sites and $H_I \in \mathbb{C}^{N\times N}$ the interaction Hamiltonian between adjacent slices. The wavevector $k \equiv k_x$ points in propagation direction. To efficiently solve the large but sparse eigenvalue problem of Eq. (2) for eigenvalues $E_n(k)$ and eigenvectors ψ_n close to the Fermi edge at a large number of k-points, we use the Lanczos method[38, 39] as implemented by the ARPACK library[40]. One of the advantages of the present approach is that its computational cost scales only with N_K^3 (N_K the dimension of the Krylov space) rather than with the number of sites N^3, $N_K \ll N$ (for details see Appendix B).

For each Bloch eigenstate ψ_n the associated group velocity in propagation direction follows from [41]

$$v_g^{(n)} = \frac{1}{\hbar}\frac{\partial E_n(k)}{\partial k} = \frac{\mathrm{i}\Delta x}{\hbar}\psi_n^\dagger\left(H_I \mathrm{e}^{\mathrm{i}k\Delta x} - \mathrm{e}^{-\mathrm{i}k\Delta x}H_I^\dagger\right)\psi_n. \quad (3)$$

To efficiently calculate the conductance as function of the energy E, we weight each Bloch state moving in $+x$-direction of the Brillouin zone, Eq. (2), with the appropriate group velocity, Eq. (3). This weighted density provides an accurate estimate for the conductance $G(E)$ by approximating the number of modes $M(E)$ at each energy,

$$G(E) = \frac{e^2}{h}M(E) \approx \frac{e^2}{h}\frac{\mathrm{d}}{\mathrm{d}E}\sum_{n:\,E_n<E}\hbar v_g^{(n)}\,\Delta k \quad (4)$$

with a k-point spacing Δk (see Appendix B). Use of Eq. (4) greatly reduces the computational cost as compared to calculations of $G(E)$ using the Landau-Büttiker formalism [42, 43], as it relies on matrix factorization instead of matrix inversion. The resulting conductance $G(E)$ converges to the Landau-Büttiker conductance at fine Δk sampling for any translationally invariant system (see Appendix B).

As our simulation is based on the band structure, the energy axis can be readily transformed into the charge carrier density by counting bands. We set $n = 0$ at the charge neutrality point $E = 0$ of graphene and express n in units of $n_0 = 1/S$, the density of one electron per moiré cell. Likewise, the magnetic field strength B is conveniently expressed in units of magnetic flux quanta through one moiré supercell Φ/Φ_0.

The large-scale band structure at zero field (Fig. 2a) features the Dirac cones with linear dispersion emanating from the K and K' points. The prominent gap at about $E_{SD} \approx -\hbar\pi/a_S v_g \approx -120$ meV is caused by the interaction of the primary cones with the backfolded satellite Dirac (SD) cones generated by the moiré potential the strength of which also controls its width $\Delta_m \approx 20$ meV. For a generic strong magnetic field ($B = 20$ T, or $\Phi/\Phi_0 = 0.851$) chosen not to coincide with a low-order rational $B_{p/q}$, flat bands associated with a multitude of Landau levels with small group velocities dominate the band structure (Fig. 2b), with a strongly increased number of gaps opening compared to the field-free case. The resulting density of states features pronounced sharp peaks (Fig. 2b). However, a further increase of the magnetic field to $B = 23.5$ T corresponding to $B_{p/q} = B_1$ (or $\Phi = \Phi_0$) leads to a dispersion (Fig. 2c) locally closely resembling the original zero-field band structure (Fig. 2a). Most notably, a clustering of Landau subbands with linear slopes approximating the slope of the original Dirac cone $v_g \approx v_F$ is observed. It signals the appearance of Brown-Zak fermions (BZfs) when magneto-translational invariance for rational fractions of the flux quantum is restored. The width in energy of the segments over which the linear dispersion of BZfs is visible remains, however, limited by the strength of the moiré potential and is of the

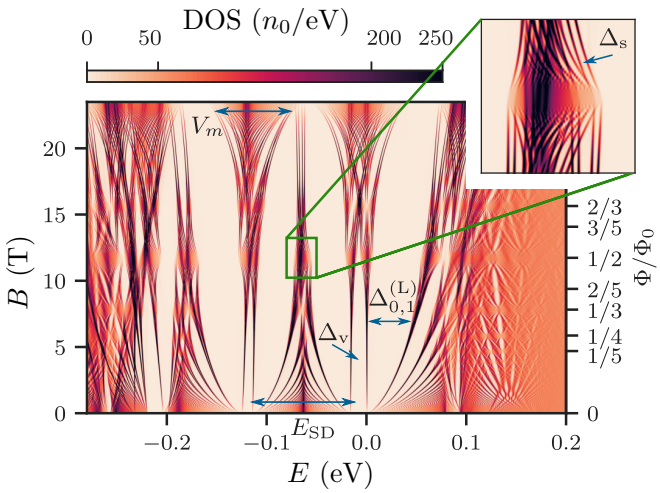

FIG. 3. Density of states (DOS) map as a function of E and B featuring multiple energy scales: E_{SD}: the spacing between the main Dirac cone and moiré induced replica, $\Delta_{n-1,n}^{(L)}$: Landau gaps, Δ_v: broken valley degeneracy, Δ_s: spin splitting, V_m: broadening by moiré potential near rational Φ/Φ_0, Inset: zoom into the intersection between Landau level $t = -1$ of the main Dirac cone and the hole satellite $\Phi/\Phi_0 = 1/2$.

order of 20 meV. The zero-field band structure and its slopes are therefore only approximately recovered. This perturbative effect of the moiré potential is fundamentally different from BZf spectra in pristine lattices where the zero-field band structure is fully recovered [44]. At large B, the large gaps between the lowest Landau levels are filled by only two quantum Hall edge states, one for each propagation direction, see, e.g., gapped regions at $E \approx 0.07$ eV in Figs. 2(b,c). Smaller gaps remain clearly visible for higher-lying Landau levels (Fig. 2c).

The density of states (DOS) map (Fig. 3) in the $E - B$ plane not only features prominent Landau gaps easily recognized by the $\sqrt{B}$ dependence of Landau levels of Dirac particles, but also multiple energy scales in the presence of both the moiré potential and the magnetic field: the moiré-induced secondary Dirac cone at $E_{\mathrm{SD}} \approx -\hbar\pi/a_S v_g \approx -120$ meV, the "broadening" of the Landau levels by $\lesssim 20$ meV at rational Φ/Φ_0 (see, e.g., inset near $\Phi/\Phi_0 = 1/2$) caused by the formation of the Hofstadter butterfly and determined by the amplitude V_m of the moiré potential, the lifting of the valley degeneracy by the moiré potential, $\Delta_V \approx 17$ meV, and of the spin degeneracy by the Zeeman term Δ_S ($\lesssim 3$ meV at $\Phi = \Phi_0$).

The simultaneous presence of multiple energy (and length) scales gives rise to a conductance map of surprising complexity. Displayed as a function of normalized flux Φ/Φ_0 and normalized carrier density n/n_0 (Fig. 4) it features several lines of low and high conductance. Lines of high conductance are strictly horizontal at fixed B and appear prominently in the projection onto the B (or Φ/Φ_0) axis (Fig. 4c). $\langle G(B)\rangle$ is clearly dominated by a sequence of peaks at rational fractions p/q of Φ/Φ_0 and is periodic in $1/B$, the so-called Brown-Zak oscillations [7–9]. Each conductance peak is associated with the ballistic transport of a BZf. The width of each peak is controlled by the effective field $B_{\mathrm{eff}} = B - B_{p/q}$. Ballistic transport is suppressed when the effective magnetic length $\lambda_{B_{\mathrm{eff}}} = \sqrt{\hbar/(eB_{\mathrm{eff}})}$ becomes smaller than the ribbon width $\lambda_{B_{\mathrm{eff}}} \ll W$. In agreement with experiments[10–15, 45], we observe an asymmetry between the electron and the hole side, which is caused by the next-nearest-neighbor graphene-substrate interlayer interaction[2].

The conductance map also features a multitude of intersecting straight lines of conductance minima, or "gaps", with different slopes, widths, and intersections with the n/n_0 axis. A subset of these gaps extend over the entire range of $0 \leq \Phi/\Phi_0 \leq 1$, while other, less prominent gaps only open for small field regions. Such gaps are conventionally described in terms of Wannier diagrams [20] which were originally developed for bandstructures with quadratic dispersion.

We analyze in the following the Wannier diagrams for pristine graphene and graphene on hBN. For a system with Schrödinger-like quadratic dispersion originally considered by Hofstadter [3] and Wannier [20], the Landau level energies evolve as function of B according to $E_t^{(S)}(B) = \hbar\omega_B(t + 1/2)$ with $t \in \mathbb{N}$ and $\omega_B = eB/m$ the cyclotron frequency. Consequently, the gaps between Landau levels $t-1$ and t are centered at $E_{g,t}^{(S)} = \hbar\omega_B t$. The normalized charge carrier density up to the Landau gap t follows in form of a Diophantine equation as

$$\frac{n}{n_0} = \int_0^{E_{g,t}^{(S)}} \rho^{(S)}(E)\,\mathrm{d}E + gs = g\left(t\frac{\Phi}{\Phi_0} + s\right) \qquad (5)$$

with s the number of filled bands at $E_0 = 0$, g the degeneracy and $\rho(E) = g/(2\pi)$ the constant density of states for fermions with quadratic dispersion in two dimensions. By contrast, the linear dispersion of massless Dirac (D) fermions results in the Landau levels at $E_t^{(D)}(B) = \mathrm{sgn}(t) v_{\mathrm{F}}\sqrt{2\hbar\,|teB|}$ with $t \in \mathbb{Z}$. Here, $t = 0$ corresponds to the zero-energy Landau level, a feature specific to Dirac fermions [46, 47]. Taking into account the linear increase of the density of states near the Dirac point, $\rho^{(D)} \propto |E|$, an analogous calculation immediately yields a modified Diophantine equation for Landau level gaps of graphene near the charge neutrality point, the *half-integer* Wannier equation

$$\frac{n}{n_0} = g^{(D)}\left(\left(t + \frac{1}{2}\right)\cdot\frac{\Phi}{\Phi_0} + s\right), \qquad s, t \in \mathbb{Z}. \qquad (6)$$

Here, $g^{(D)}$ denotes the degeneracy of the graphene levels and is $g^{(D)} = 4$ for full valley and spin degeneracy. The present results are fully consistent with the characteristic "half-integer" Quantum Hall conductance [46, 47] $\sigma_{xy} = g^{(D)}(t + 1/2)\,e^2/h$, $t \in \mathbb{Z}$ of graphene. For massless Dirac fermions the minimal degeneracy is $g^{(D)} \geq 2$ due to fermion doubling as consequence of the Nielsen–Ninomiya theorem[48] realized as valley degeneracy in graphene. Thus, the gaps described by Eq. (6) are, despite the half-integer slopes $(t + 1/2)$, *always* a proper subset of those resulting from Eq. (5). Moreover, the slopes t of the gaps in the Wannier diagram field can be related to the Hall conductivity $\sigma_{xy} = e\partial n/\partial B|_{E=E_F} = -C \cdot e^2/h$ [21, 49] with Chern number C.

To illustrate the differences and similarities between Wannier diagrams emerging for Schrödinger-like and Dirac-like

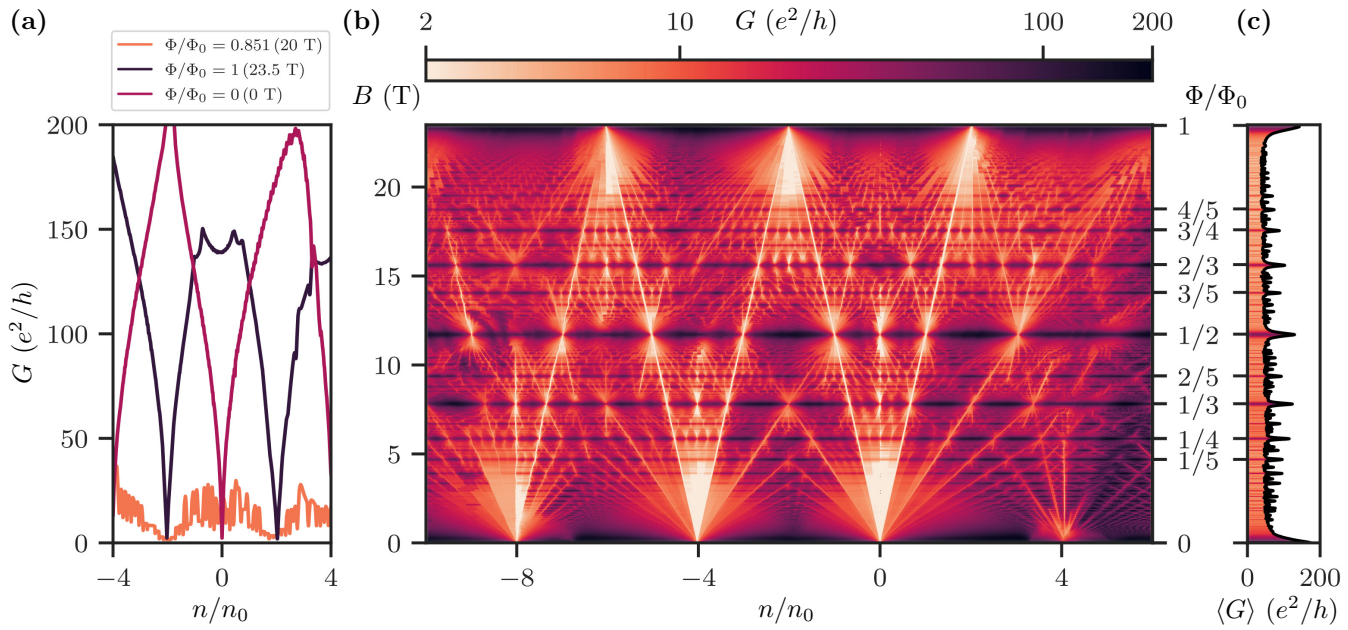

FIG. 4. (a) Conductance traces of a 750 nm wide graphene nanoribbon on hBN at specific magnetic fields of $B = 0$, $B = 20$, $B = 23.5$ T. (b) Conductance map $G(n/n_0, B)$. Landau gaps appear as light, tilted lines, and Brown Zak oscillations as dark horizontal lines. The vertical axis Φ/Φ_0 on the rhs denotes the normalized flux per moiré unit cell. (c) The conductance map projected onto the B-axis $\langle G(B) \rangle$ shows pronounced Brown Zak oscillations periodic in $1/B$.

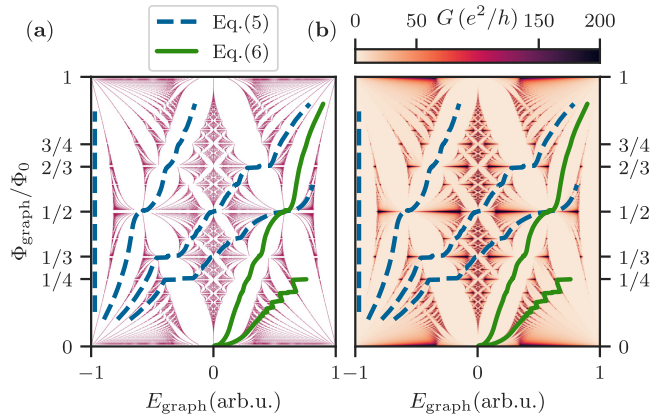

FIG. 5. Pristine graphene lattice at strong magnetic fields: (a) The Hofstadter butterfly of a pristine hexagonal lattice (eigenvalues in purple). (b) The conductance map of a pristine graphene nanoribbon $G(E, \Phi/\Phi_{0,\text{graph}})$. The overlayed lines show all Landau gaps predicted by the Schrödinger-like Diophantine equation Eq. (5) (blue-dashed lines, $t = 0, 1, 2, 3$) and the subset predicted by the Dirac Diophantine equation Eq. (6) (green solid lines, $t = 0, 1$) for the same range of positive slopes ($0 \leq \mathrm{d}n/\mathrm{d}\Phi \leq 3n_0/\Phi_0$). Spin neglected for simplicity.

dispersion, a comparison with the Wannier diagram of the pristine honeycomb lattice [Fig. 5] is instructive. We note that the required magnetic field to achieve a magnetic flux quantum Φ_0 through a single unit cell of the graphene honeycomb is orders of magnitude larger than for the moiré supercell due to the difference in area of the unit cell. In the following we denote quantities related to pristine graphene (as opposed to graphene on hBN) by the subscript *graph*. Pristine graphene features a parabolic dispersion near the band maxima and minima ($E_{\text{graph}} = \pm 1$), but a linear (Dirac-like) dispersion at the Dirac points ($E_{\text{graph}} = 0$). Accordingly, the Hofstadter butterfly (energy eigenvalues as function of magnetic flux [4, 50, 51]) of the hexagonal lattice (Fig. 5 (a)) features around $E_{\text{graph}} = 0$ only those gaps described by the half-integer formula of Eq. (6), while all gaps near $E_{\text{graph}} = \pm 1$ follow the usual Schrödinger-like formula [Eq. (5)] Additional lines in Fig. 5 mark selected gaps emerging from ($E_{\text{graph}} = -1$, $\Phi_{\text{graph}} = 0$) (dashed blue lines) and ($E_{\text{graph}} = 0$, $\Phi_{\text{graph}} = 0$) (green solid lines). Schrödinger-like and Dirac-like Landau fans are closely intertwined. Gaps emanating from the Dirac point at $E_{\text{graph}} = 0$ for $\Phi = 0$ continuously evolve into gaps forming Schrödinger-like Landau fans at $E_{\text{graph}} = \pm 1$ and $\Phi_{\text{graph}} = \Phi_0$ and vice versa. This connection reflects the observation that the lines predicted by Eq. (6) form a proper subset of those predicted by Eq. (5). Indeed, there are lines predicted only by Eq. (5) but not by Eq. (6) connecting a Schrödinger-like Landau fan at $\Phi_{\text{graph}} = 0$ with another one at $\Phi_{\text{graph}} = \Phi_0$, for example the vertical lines at $E_{\text{graph}} = \pm 1$. By contrast, a similar vertical line from $\Phi_{\text{graph}} = 0$ to $\Phi_{\text{graph}} = \Phi_0$ at $E_{\text{graph}} = 0$ is missing.

The conductance signal for the pristine graphene ribbon Fig 5 (b) closely mirrors the eigenvalue map Fig 5 (a). Energy gaps between eigenvalues now appear as regions of low conductance while regions densely populated with eigenvalues correlate with a larger conductance. Resulting density enhancements along horizontal lines with rational flux

$\Phi_{\text{graph}}/\Phi_0$ give rise to Brown-Zak oscillations.

After rescaling the energy axis to a density axis we can directly compare the resulting Wannier diagram for pristine graphene (Fig. 6a) with that for the moiré-induced supercell of graphene on hBN (Fig. 6b). It is important to realize that the Wannier diagram for the superlattice represents the magnification of a small region near $\Phi_{\text{graph}}/\Phi_0 = 0$ and near the Dirac point $E_{\text{graph}} \approx 0$ of the diagram for pristine graphene Fig. 6a. This is because the scale of the Wannier diagram is determined by the magnetic flux through a unit cell as well as the electron density n normalized to a unit cell (denoted by n_0 for the moiré supercell of graphene on hBN and by $n_{0,\text{graph}}$ for pristine graphene). The most prominent difference are the Dirac satellite cones with spacings of $n/n_0 = 4$ in the presence of the moiré potential (Fig. 6b), which are absent in the case of pristine graphene (Fig. 6a). The Wannier diagram for the moiré superlattice is therefore, unlike for pristine graphene, not periodic in Φ with period Φ_0. Periodicity is broken because the lateral spacing between the Dirac fans of the satellite conses is $4(n/n_0)$ while the minimum slope in the Dirac diophantine equation [Eq. (6)] is 2. Consequently, the fans at $0, \pm 4(n/n_0), \ldots$ at $\Phi/\Phi_0 = 0$ connect to fans at $\pm 2, \pm 6, \ldots (n/n_0)$ at $\Phi/\Phi_0 = 1$. Correspondingly, lines that would reach $n/n_0 = 0, \pm 4$ at $\Phi = \Phi_0$ are missing. Such a non-periodicity is clearly visible in recent experiments (see App. C).

The Wannier diagram for the moiré superlattice reveals that weakly lifting the valley degeneracy by the interaction with hBN and the spin degeneracy by the Zeeman interaction locally generates additional gaps that follow the conventional Diophantine equation (Eq. 5) with $g = 1$ [see blue dashed lines in Fig. 6 (b)]. Since the energy scale V_m of the moiré potential forming the BZfs is large compared to the valley splitting Δ_v and spin splitting Δ_s generating these gaps, the additional gaps persist only for small intervals of the magnetic field. Consequently, the additional lines predicted by Eq. (5) disappear when passing through nearby BZfs at rational Φ/Φ_0. By contrast, the Dirac-like Landau gaps predicted by Eq. (6) persist over the full magnetic field range [solid green lines in Fig. 6(b)], resulting in the non-periodic Wannier diagram.

A comparison with recent experiments [14, 17] confirms all our qualitative predictions (see App. C), including the broken periodicity in Φ_0, the Wannier gaps predicted for Dirac fermions, Eq. (6), and the local re-appearance of additional gaps following Eq. (5) near crossing points in the Wannier diagram. Note that our approach is based on an effective single-particle description on the DFT level without invoking any many-body effects. Our results can thus serve as benchmark to identify true many-body physics beyond the single-particle picture in experimental data. The energy scale for many-body effects, Δ_{MB}, can be estimated from the flat bands in magic angle twisted bilayer graphene [52, 53] and from measurements on bilayer graphene quantum dots[54] to be $\Delta_{\text{MB}} \lesssim 1$ meV and, thus, smaller than the energy scales shaping the structures in the Wannier diagram (Figs. 4 and 6b) in the present case.

In conclusion, we have shown that Hofstadter's butterfly in graphene (pristine and aligned on hBN) follows a half-integer Wannier equation for Landau gaps of massless Dirac particles. When valley and spin degeneracy are broken by the hBN substrate, a fine structure emerges that locally follows Wannier's equation for Schrödinger-like particles. This Wannier description agrees with our highly accurate conductance simulation of the graphene on hBN system. Our simulations further show in detail the emergence of Brown-Zak fermions in moiré superlattices.

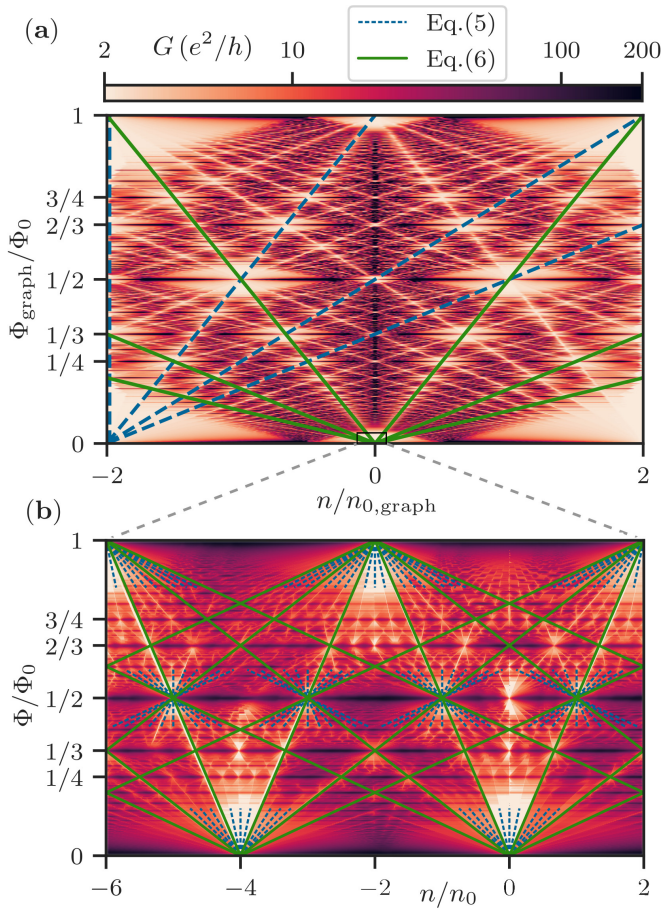

FIG. 6. Comparison between the Wannier diagram for pristine graphene (a) and for graphene on hBN (b). Shown is the conductance map $G(n/n_0, \Phi/\Phi_0)$ with an overlay of the Landau gaps predicted by the Schrödinger-like Diophantine equation Eq. (5) (blue-dashed lines) and by the Dirac Diophantine equation Eq. (6) (green solid lines). The six green solid lines emanating from $n = 0$ are the same in (a) and (b). G at fixed n/n_0 is periodic in Φ/Φ_0 in (a) but not in (b) because the satellite cones break the periodicity. Note that the range of magnetic field and density values covered by (b) is only a very small fraction of those covered by (a), schematically indicated by the (not to scale) box in (a): $n/n_0 \approx 1.5 \times 10^{-4} n/n_{\text{graph}}$. The range $-2 \leq n \leq 2$ is due to the $g = 4$ degeneracy of graphene.

ACKNOWLEDGMENTS

We thank T. Jawecki and C. Stampfer for helpful discussions. The computational results presented have been achieved using the Vienna Scientific Cluster (VSC4). Fig. (6 a) was computed with pybinding.[55]

Appendix A: Tight-binding model details

Several model Hamiltonians for describing graphene on hexagonal boron nitride (hBN) have been proposed, often with a strong focus on quantitative prediction of band gaps or the lowest-energy bands at zero or low magnetic fields [25, 28, 56–59]. We combine an atomistic tight-binding Hamiltonian parametrized from density functional theory (DFT) and a mechanical strain model to correctly account for strong magnetic fields (one flux quantum per moiré unit cell). To derive an ab-initio atomistic model for the moiré superstructure of graphene on hexagnoal boron nitride (hBN), we first calculate an atomic reconstruction using elasticity theory and – in a second step – set each tight-binding parameter based on the local atomic alignment as simulated by a primitive-cell DFT calculations. In the following we briefly sketch the details of the model.

1. Rigid supercell

The lattice constants of graphene and hBN differ by $\approx 1.7\%$ [28], preventing exact commensurabilty of perfectly aligned hBN/graphene of any size still accessible by tight-binding. To reach an approximate commensurability we therefore fix our model to a hexagonal supercell containing 58×58 graphene unit cells and 57×57 hBN unit cells, setting the lattice constants to 2.461 Å for graphene and 2.5042 Å for hBN. To obtain parameters for the different relative atomic configurations within the large supercell, we consider primitive cells (i.e. 4 atoms) with a corresponding relative shift $\vec{d}$ between the graphene and hBN layer. We first map primitive-cell tight-binding parameters as a function of $\vec{d}$ using DFT, and then assemble a Hamiltonian for the entire superstructure.

2. DFT calculation details

We perform ab-inito calculations for two different systems: 1.) Strain-dependent single-layer cells for the elasticity model describing the layer relaxation (see next subsection) and 2.) stacking dependent primitive bilayer cells. Each of the cells is calculated using VASP within the local density approximation (LDA)[32], together with a k-mesh of $25 \times 25 \times 1$ on a Monkhorst pack grid, an energy cutoff of 380 eV and 25 Å vacuum in z-direction.

a. Primitive cell hBN/graphene bilayer calculations

We map the 2-dimensional configuration space of $\vec{d}$ using a 10×10 grid, resulting in 100 primitive bilayer cells. Each with a top layer shifted relative to the bottom layer by $\vec{d} = \vec{a}_1 u/10 + \vec{a}_2 v/10$ with $u, v \in \{0, \dots, 9\}$, where $\vec{d} = 0$ has AA stacking (see Fig. 7 (a)) and $\vec{a}_1$ and $\vec{a}_2$ are the supercell lattice vectors. For the hBN/graphene calculations we use a primitive unit cell of 2.48Å. The atomic positions were allowed to relax in out-of-plane direction but remain fixed in-plane. Subsequently, we project the Kohn-Sham orbitals onto the p_z carbon-orbitals via a Wannier transformation [61, 62]. Note that we only include one p_z orbital per carbon atom. We thus exclude boron and nitrogen orbitals as well as the σ and σ^* of graphene, since they do not directly contribute to transport around the Fermi energy. For treating higher-lying regions of the band structure, they would have to be included [28].

Restricting the tight-binding parametrization to two orbitals in the graphene layer allows mapping the coupling as a function of $\vec{d}$, as each coupling element is periodic under lateral translations along $\vec{a}_1$ and $\vec{a}_2$ (see example in Fig. 7 (b)). This periodicity would be broken for materials with interlayer terms (e.g. in twisted bilayer graphene). For the system at hand we can therefore express the stacking dependence of each tight-binding hoping matrix element in terms of a Fourier expansion,

$$\hat{t}_{i,j}^{\vec{G}} = \sum_{\vec{d}} t_{i,j}(\vec{d}) \cdot \mathrm{e}^{i\vec{d}\cdot\vec{G}} \tag{A1}$$

with $\vec{G} = m\vec{G}_1 + n\vec{G}_2$ for all m, n. Including the Fourier components with $|\vec{G}| \leq 2 \cdot |\vec{G}_1|$, is sufficient to resemble the modulation of $\hat{t}_{i,j}^{\vec{G}}$ as a function of $\vec{d}$ (see Fig. 7 (c) and (d)). Similar to the coupling elements $t_{i,j}$ we parametrize the generalized stacking fault energies (GSFEs) in terms of the Fourier expansion, [28, 34, 35],

$$E(\vec{d}) = \sum_{\vec{G}} c_{\vec{G}} e^{i\vec{d}\vec{G}}, \tag{A2}$$

describing the dependence of the DFT energy on the relative alignment of the layers. The GSFE is utilized in the calculation of the in-plane lattice relaxation (see (C)).

b. Strain dependent single layer graphene calculations

In order to account for the considerable strain present in the reconstructed graphene supercell, we additionally introduce a local strain dependent correction to the couplings,

$$t_{i,j} \to t_{i,j} \mathrm{e}^{-(l-l_0)\alpha_{i,j}}. \tag{A3}$$

The α's are determined based on single layer strain dependent uniform graphene calculations and fitted to the dependence of the $t_{i,j}$ (taken from Wannier orbitals) on the lattice constant around the equilibrium lattice constant of graphene (2.461Å). For the DFT calculations similar specifications as for the stacking dependent terms were used.

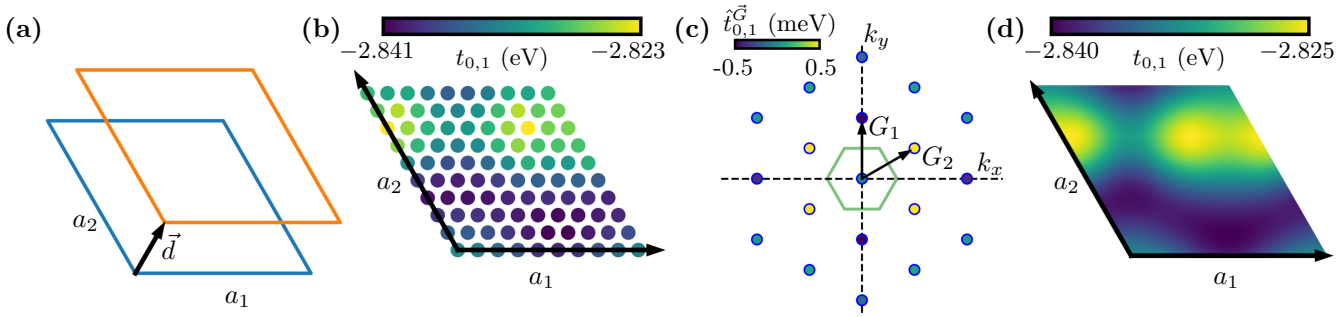

FIG. 7. Stacking dependence of tight-binding coupling elements. (a) frames of the graphene (orange) and hBN (blue) primitive unit-cells, the black arrow indicates their relative shift $\vec{d}$. (b) Example of one coupling element $t_{0,1}(\vec{d})$ for different translation vectors $\vec{d}$ within the unit cell spanned by $\vec{a}_1$ and $\vec{a}_2$. (c) reciprocal representation of (b). (d) Representation of (b) by low-order Fourier components ($|\vec{G}| < 2 \cdot |\vec{G}_1|$) only and dropping the zeroth component.

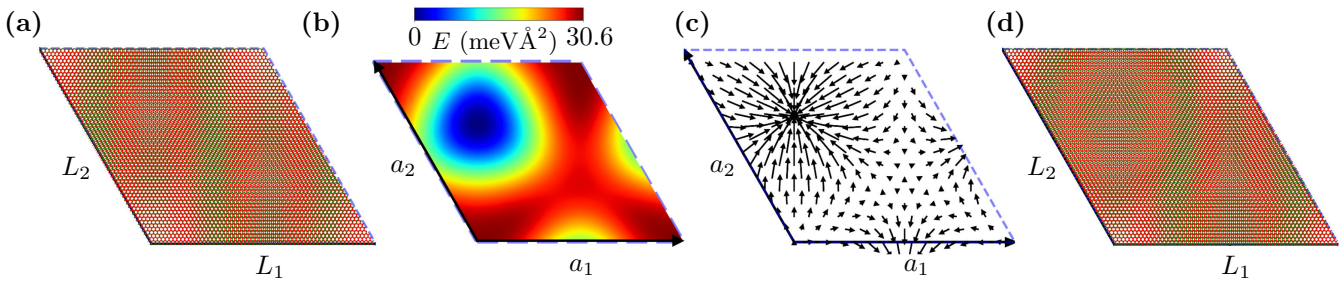

FIG. 8. Graphene on hBN supercell and its lattice reconstruction. (a) geometry of rigid graphene on hBN. (b) energy landscape (generalized stacking fault energy) of the stacking configuration. (c) reconstruction of atomic positions. The arrows indicate the relative displacement at a given stacking position. (d) geometry of the reconstructed graphene hBN supercell, providing a similar structure as recently observed by STM [60].

3. Relaxation

In a hBN/graphene heterostructure, certain local configuration of atoms are energetically more favourable than others, resulting in considerable lattice reconstruction[60, 63]. This lattice reconstruction can be split into an out-of-plane part defining the local distance between the layers and an in-plane part causing a local sliding of atoms in lateral direction. The latter is by orders of magnitude larger (see discussion below), allowing to treat the in-plane and out-of-plane relaxation independently. Our approach for the in-plane lattice reconstruction follows closely an elasticity model described by Nam et al. [35] for twisted bilayer graphene. In such an approach, the equilibrium between energy gain due to a smaller stacking fault energy and elastic energy costs for lattice deformation is determined. Our energy functional depends on the local displacement vectors $\vec{u}_i(\vec{r})$ with i = hBN, G for the two layers. It reads

$$U_{\text{tot}} = U_E[\vec{u}_{\text{hBN}}] + U_E[\vec{u}_{\text{G}}] + U_B[\vec{u}_{\text{hBN}}, \vec{u}_{\text{G}}]. \tag{A4}$$

The stacking dependence of the potential energy is parametrized via the generalized stacking fault energy, using the Fourier components $c_{\vec{G}}$ of Eq. A2,

$$\text{U}_\text{B}[\vec{u}^{\text{hBN}}, \vec{u}^{\text{G}}] = \int d\vec{r} \sum_{\vec{G}} c_{\vec{G}} \exp\left[i\left(\vec{d} + \Delta\vec{u}\right) \cdot \vec{G}\right]$$

with $\Delta\vec{u} = (\vec{u}^{\text{hBN}} - \vec{u}^{\text{G}})$. The intra-layer energy U_E describing the elastic energy as defined in Eq. (25) of Ref. [35], is given by

$$\text{U}_\text{E}[\vec{u}^{\,l=\text{G/hBN}}] = \int d\vec{r} \left[\frac{\lambda_l + \mu_l}{2} \left(\frac{\partial \vec{u}^l_x}{\partial x} + \frac{\partial \vec{u}^l_y}{\partial y} \right)^2 + \frac{\mu_l}{2} \left(\frac{\partial \vec{u}^l_x}{\partial x} - \frac{\partial \vec{u}^l_y}{\partial y} \right)^2 + \frac{\mu_l}{2} \left(\frac{\partial \vec{u}^l_x}{\partial y} + \frac{\partial \vec{u}^l_y}{\partial x} \right)^2 \right]. \tag{A5}$$

We use Lamé parameters in units of eV/Å^2] $\lambda_\text{G} = 3.25$ and $\mu_\text{G} = 9.57$ for graphene and $\lambda_{\text{hBN}} = 3.5$ and $\mu_{\text{hBN}} = 7.8$ [28, 59, 64] for hBN. This energy functional is most conveniently minimized by utilizing a variant of the minimzation procedure described by Nam et al.[35]. Minimizing the energy functional (Eq. (A4)) suggests the AB stacking configuration (one boron atom above one carbon atom) as the energetically most favourable lattice alignment (see Fig. 8 (c)) resulting in significant increase in the area of this stacking configuration (compare Fig. 8 (a) and (b)).

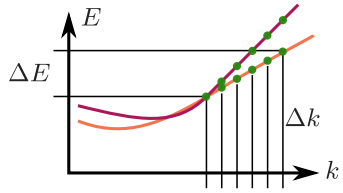

FIG. 9. Sampling a band structure, schematically. Bands $E_n(k)$ in purple and orange, are "sampled" equidistantly in k-space at the green dots $E_n(j \cdot \Delta k)$. In an energy interval ΔE, more points from the flatter (orange) than for the steeper (red) band are sampled. The density of states, Eq. (B4), corresponds to counting the number of points in an energy interval ΔE. To estimate the number of bands in an energy interval ΔE, Eq. (B2), one has to weight each sampled point on the k axis by the associated slope, i.e., the corresponding group velocity, which is larger for the steeper line.

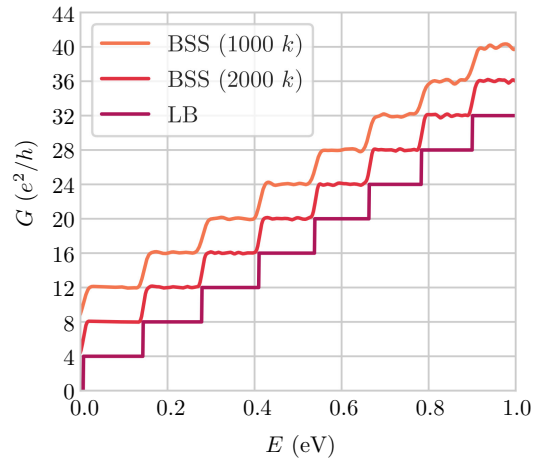

FIG. 10. Conductance G as a function of energy of an 18 nm wide graphene ribbon calculated in Landauer-Büttiker formalism ("LB", purple), and with help of the band structure sampling. Shown are a calculations by band structure sampling (BSS) Eq. (B2) with 2000 k-points ("BSS (2000 k)", red), offset by $4e^2/h$, and 1000 k-points ("BSS (1000 k)", orange), offset by $8e^2/h$. BSS curves are smoothed to remove artifacts of the k-point sampling while still retaining as much detail (conductance steps) as possible.

4. Tight-Binding parameters

Accounting for the two main effects influencing the graphene/hBN lattice, namely the presence of a hBN layer and the induced strain, we model the influence of the hBN layer on the graphene layer by a stacking dependent tight-binding parameter $t_{i,j}(\vec{d})$ and the strain dependence by Eq. (A3)

$$t_{i,j}(\vec{d}, l) = t_{i,j}(\vec{d}) \mathrm{e}^{-(l-l_0)\alpha_{i,j}}. \tag{A6}$$

Here $\vec{d}$ describes the relative alignment of the two layers relative to AA stacking, l the effective distance between the orbitals i and j and l_0 the corresponding unstrained distance. We fit the scaling function $\alpha_{i,j}$ in the exponential to the DFT results for single graphene layer.

Appendix B: Computing the conductance from a band structure

The key results presented in the main text required the evalutaion of the conductance of the graphene on hBN moiré, a veritably huge system by all numerical standards, by a novel approach. Our approach relies on the fact that the conductance as a function of energy $G(E)$ of a strictly periodic, translationally invariant nanoribbon (see Fig. 1) is proportional to the number of open modes propagating in $+x$ direction $M(E)$ [65], $G(E) = \frac{e^2}{h} M(E)$.

In general, it is a formidable task to solve for the number of open modes at a given energy, since the recursive Greens function formalism (used in the standard Landauer-Büttiker calculation) scales with the number of basis functions in the unit cell of the ribbon N as $\mathcal{O}(N^3)$. By contrast, calculating the band structure only requires eigenvalues around the charge neutrality point of a sparse matrix for a given k, readily allowing for iterative schemes. We need to solve the eigenvalue problem of Eq. 2, which we write for brevity as

$$H(k)\psi_n = E_n(k)\,\psi_n, \tag{B1}$$

Using shift-and-invert in conjunction with the Lanczos method, we calculate about 100 energy eigenvalues $E_n(k)$ of the band structure with a single matrix factorization — we factorize at several energy values to cover the energy range $E \approx [-0.3, 0.3]$ eV.

The difficulty now lies in determining the number of modes propagating in $+x$ direction from a discrete set of eigenvalues $E_n(j \cdot \Delta k)$, $j \in \mathbb{N}$ for a given resolution Δk in reciprocal space. We use the sign of the group velocities $v_g = \hbar \partial E / \partial k > 0$ to select and properly map the number of bands from the k-axis onto the number of modes propagating in $+x$-direction M on the energy axis,

$$\begin{aligned} M(E) &\approx \sum_{m=1}^{M} \frac{\partial E}{\partial k} \frac{\Delta k}{\Delta E} \\ &\approx \frac{\mathrm{d}}{\mathrm{d}E} \sum_{n:\, E_n < E,\, v_g^{(n)} > 0} \hbar v_g^{(n)} \cdot \Delta k. \end{aligned} \tag{B2}$$

The summation runs over all eigenvalues E_n with energy smaller than E. We obtain a histogram of the band structure, weighted by the group velocities (Fig. 9). To reduce the effect of binning, we evaluate Eq. (B2) in terms of an energy derivative of a smoothed density obtained from interpolating the discrete sum.

We compare the present band structure sampling method for extracting the conductance from properties of the band structure with the conventional method using the standard Landauer-Büttiker (LB) [42, 43, 66, 67] formalism. The present method approximates the conductance trace of a 18 nm wide graphene nanoribbon (for which the computationally more demanding Landauer-Büttiker formalism still can be applied) with remarkable accuracy (Fig. 10). The accuracy of

Eq. B2 depends on the number of k-points N_{kpt} used. Its precision can be increased by a finer sampling of the band structure; shown here are sampling of $N_{\mathrm{kpt}} = 1000$ and $N_{\mathrm{kpt}} = 2000$. We find suitable convergence of the conductance (i.e., no further noticeable change upon further increasing N_{kpt}) for $N_{\mathrm{kpt}} = 3000$, which we use for all final results.

Obtaining an accurate conductance requires evaluating the band structure at a large number N_{kpt} of k-points. To further improve the efficiency of our Krylov-space approach, we exploit the continuity of the band structure for small variations in k. Instead of solving the Bloch eigenvalue problem for all N_{kpt} k-points, we calculate a Krylov-space for an evenly spaced subset $\{k_i\}$, $i = 1 \dots N_{\mathrm{kS}}$ with $N_{\mathrm{kS}} \ll N_{\mathrm{kpt}}$ k-points. We then combine the subspaces of two adjacent k-values k_i and k_{i+1} to form a basis $\{b_i\}$ spanning the eigenvectors of both Krylov spaces. We can now readily evaluate the band structure for densely-spaced intermediate k values $k_i \leq k \leq k_{i+1}$ by projection onto the basis $\{b_i\}$. An initial coarse sampling of the Brillouin zone N_{kS} is thus sufficient to obtain an excellent k-resolution of the band structure. Unphysical eigenvalues that appear because of the larger size of the combined subspace are efficiently identified by evaluating the error norm

$$\delta_n = \sum_i \left| \phi_i \left[H(k) - E_n(k) \mathbb{1} \right] \psi_n \right|^2 \tag{B3}$$

for a set of randomly chosen vectors $\phi_i \in \mathbb{C}^N$ with $i = 1, \dots, N_K$ that heuristically sample the full eigenvalue equation. δ_n is zero only for a true eigenvector of the full problem. The projections of ϕ_i on H_0 and H_I are k-independent and thus need only be evaluated once.

Analogously, the density of states can be extracted by sampling the band structures for the conductance,

$$\rho(E) \approx \frac{\mathrm{d}}{\mathrm{d}E} \sum_{n:\, E_n < E} \Delta k. \tag{B4}$$

We emphasize that Brown-Zak oscillations are not visible in the density of states (Fig. 2), because of the broadening of the Landau levels and associated smearing of the density of states. Peaks induced by Brown-Zak oscillations only appear in the conductance after weighting the sum in Eq. (B4) by the group velocities (Eq. (B2)).

Appendix C: Comparison with the experiment

The Wannier diagram of the Landau gaps of graphene on hexagonal boron nitride close to charge neutrality [Eq. (6)]

$$\frac{n}{n_0} = 4 \left(\left(t + \frac{1}{2} \right) \cdot \frac{\Phi}{\Phi_0} + s \right), \qquad s, t \in \mathbb{Z} \tag{C1}$$

provides a natural explanation for the evolution of the large Landau gaps in recent measurements. We overlay the gaps according to Eq. (6) on the data obtained by Wang et al.[14] (Fig. 11) and Barrier et al.[17] (Fig. 12). The most prominent conductance minima, or gaps, are the Landau fans emerging from $n/n_0 = \dots, -4, 0, 4, \dots$ at $\Phi/\Phi_0 = 0$ which *asymmetrically* evolve to Landau fans at $n/n_0 = \dots, -2, 2, \dots$ at

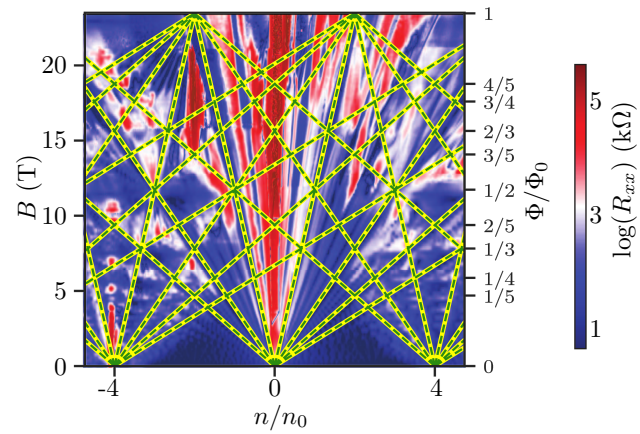

FIG. 11. Conductance of graphene aligned on hexagonal boron nitride as a function of charge carrier density and magnetic field: experimental data (color scale) taken from [14]. Lines overlayed in the yellow-green contrast colors are from Eq. (6) and give the density dependence of the Landau gaps. They display the non-periodicity in Φ of the measurement. Gaps between these Landau gaps can now be easily identified as spin- and valley gaps, compare Fig. 6b.

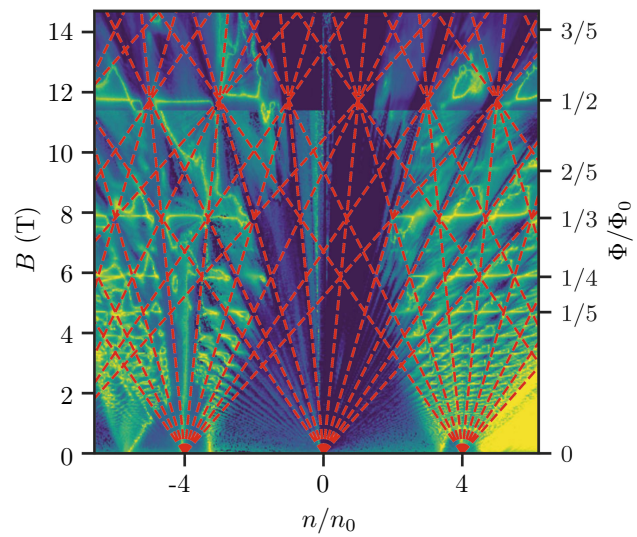

FIG. 12. Conductance of graphene aligned on hexagonal boron nitride as a function of charge carrier density and magnetic field: experimental data (color scale: "Indigo-to-yellow colors: Log scale truncated between 38 nS and 16 mS for $B < 14$ T and between 4 nS and 0.4 mS above 14 T.") taken from Barrier et al.[17]. Lines overlayed in the red are from Eq. (6) and give the density dependence of the Landau gaps. They display the non-periodicity in Φ of the measurement. Yellow horizontal lines of large conductance at rational flux signifying Brown-Zak oscillations, are broken at the densities where Landau gaps appear (compare Fig. 6(b)).

$\Phi/\Phi_0 = 1$. In both measurements, no other gaps are visible that extend over the full magnetic field range. Furthermore, smaller spin- and valley gaps (between the overlayed Landau gaps) become visible for small magnetic field ranges, e.g. in

the first and second Landau level in both experiments (compare also the data in Fig. 6b).

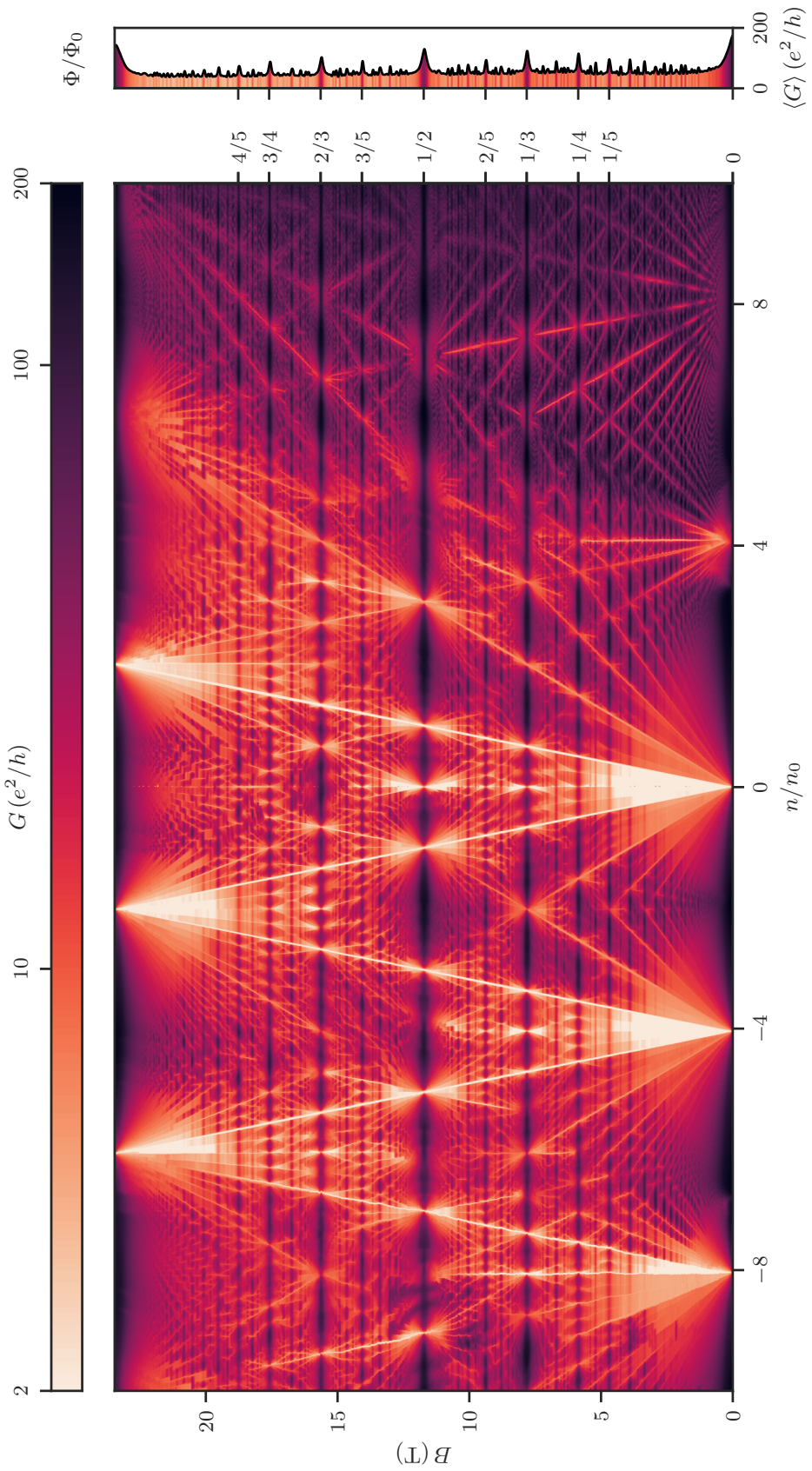

FIG. 13. (a) Conductance map $G(n/n_0, B)$ of a 750 nm wide graphene nanoribbon on hBN (same system as in Fig. 4 showing an extended charge carrier density range). Note the periodic repetition of satelite Dirac cones on the extended n/n_0 axis. Additional vertical axis Φ/Φ_0 denotes the normalized flux per moiré unit cell.

[1] C.-H. Park, L. Yang, Y.-W. Son, M. L. Cohen, and S. G. Louie, Phys. Rev. Lett. **101**, 126804 (2008).
[2] M. Yankowitz, J. Xue, D. Cormode, J. D. Sanchez-Yamagishi, K. Watanabe, T. Taniguchi, P. Jarillo-Herrero, P. Jacquod, and B. J. LeRoy, Nature Physics **8**, 382 (2012).
[3] D. R. Hofstadter, Phys. Rev. B **14**, 2239 (1976).
[4] R. Rammal, Journal de Physique **46**, 1345 (1985).
[5] A. Matulis and F. M. Peeters, Phys. Rev. B **75**, 125429 (2007).
[6] R. Huber, M.-N. Steffen, M. Drienovsky, A. Sandner, K. Watanabe, T. Taniguchi, D. Pfannkuche, D. Weiss, and J. Eroms, "Brown-zak and weiss oscillations in a gate-tunable graphene superlattice: A unified picture of miniband conductivity," (2021), arXiv:2106.11328.
[7] E. Brown, Phys. Rev. **133**, A1038 (1964).
[8] J. Zak, Phys. Rev. **134**, A1602 (1964).
[9] J. Zak, Phys. Rev. **134**, A1607 (1964).
[10] L. A. Ponomarenko, R. V. Gorbachev, G. L. Yu, D. C. Elias, R. Jalil, A. A. Patel, A. Mishchenko, A. S. Mayorov, C. R. Woods, J. R. Wallbank, M. Mucha-Kruczynski, B. A. Piot, M. Potemski, I. V. Grigorieva, K. S. Novoselov, F. Guinea, V. I. Fal'ko, and A. K. Geim, Nature **497**, 594 (2013).
[11] C. R. Dean, L. Wang, P. Maher, C. Forsythe, F. Ghahari, Y. Gao, J. Katoch, M. Ishigami, P. Moon, M. Koshino, T. Taniguchi, K. Watanabe, K. L. Shepard, J. Hone, and P. Kim, Nature **497**, 598 (2013).
[12] B. Hunt, J. D. Sanchez-Yamagishi, A. F. Young, M. Yankowitz, B. J. LeRoy, K. Watanabe, T. Taniguchi, P. Moon, M. Koshino, P. Jarillo-Herrero, and R. C. Ashoori, Science **340**, 1427 (2013), https://science.sciencemag.org/content/340/6139/1427.full.pdf.
[13] G. L. Yu, R. V. Gorbachev, J. S. Tu, A. V. Kretinin, Y. Cao, R. Jalil, F. Withers, L. A. Ponomarenko, B. A. Piot, M. Potemski, D. C. Elias, X. Chen, K. Watanabe, T. Taniguchi, I. V. Grigorieva, K. S. Novoselov, V. I. Fal'ko, A. K. Geim, and A. Mishchenko, Nature Physics **10**, 525 (2014).
[14] L. Wang, Y. Gao, B. Wen, Z. Han, T. Taniguchi, K. Watanabe, M. Koshino, J. Hone, and C. R. Dean, Science **350**, 1231 (2015), https://science.sciencemag.org/content/350/6265/1231.full.pdf.
[15] R. Krishna Kumar, X. Chen, G. H. Auton, A. Mishchenko, D. A. Bandurin, S. V. Morozov, Y. Cao, E. Khestanova, M. Ben Shalom, A. V. Kretinin, K. S. Novoselov, L. Eaves, I. V. Grigorieva, L. A. Ponomarenko, V. I. Fal'ko, and A. K. Geim, Science **357**, 181 (2017), https://science.sciencemag.org/content/357/6347/181.full.pdf.
[16] R. Krishna Kumar, A. Mishchenko, X. Chen, S. Pezzini, G. H. Auton, L. A. Ponomarenko, U. Zeitler, L. Eaves, V. I. Fal'ko, and A. K. Geim, Proceedings of the National Academy of Sciences **115**, 5135 (2018), https://www.pnas.org/content/115/20/5135.full.pdf.
[17] J. Barrier, P. Kumaravadivel, R. Krishna Kumar, L. A. Ponomarenko, N. Xin, M. Holwill, C. Mullan, M. Kim, R. V. Gorbachev, M. D. Thompson, J. R. Prance, T. Taniguchi, K. Watanabe, I. V. Grigorieva, K. S. Novoselov, A. Mishchenko, V. I. Fal'ko, A. K. Geim, and A. I. Berdyugin, Nature Communications **11**, 5756 (2020).
[18] F. Bloch, Zeitschrift für Physik **52**, 555 (1929).
[19] M. Y. Azbel, Sov. Phys. JETP **19**, 634 (1964).
[20] G. H. Wannier, physica status solidi (b) **88**, 757 (1978), https://onlinelibrary.wiley.com/doi/pdf/10.1002/pssb.2220880243.
[21] P. Streda, Journal of Physics C: Solid State Physics **15**, L717 (1982).
[22] J.-W. Rhim and K. Park, Physical Review B **86**, 235411 (2012).
[23] P. Delplace and G. Montambaux, Physical Review B **82**, 035438 (2010).
[24] X. Chen, J. R. Wallbank, A. A. Patel, M. Mucha-Kruczyński, E. McCann, and V. I. Fal'ko, Phys. Rev. B **89**, 075401 (2014).
[25] S. Carr, S. Fang, and E. Kaxiras, Nature Reviews Materials **5**, 748 (2020).
[26] L. A. Chizhova, F. Libisch, and J. Burgdörfer, Phys. Rev. B **90**, 165404 (2014).
[27] J. Jung, A. Raoux, Z. Qiao, and A. H. MacDonald, Phys. Rev. B **89**, 205414 (2014).
[28] J. Jung, A. M. DaSilva, A. H. MacDonald, and S. Adam, Nature Communications **6**, 6308 (2015).
[29] G. Chen, M. Sui, D. Wang, S. Wang, J. Jung, P. Moon, S. Adam, K. Watanabe, T. Taniguchi, S. Zhou, M. Koshino, G. Zhang, and Y. Zhang, Nano Letters **17**, 3576 (2017).
[30] M.-H. Liu, P. Rickhaus, P. Makk, E. Tóvári, R. Maurand, F. Tkatschenko, M. Weiss, C. Schönenberger, and K. Richter, Phys. Rev. Lett. **114**, 036601 (2015).
[31] S.-C. Chen, R. Kraft, R. Danneau, K. Richter, and M.-H. Liu, Communications Physics **3**, 71 (2020).
[32] G. Kresse and J. Furthmüller, Phys. Rev. B **54**, 11169 (1996).
[33] R. Bistritzer and A. H. MacDonald, Phys. Rev. B **84**, 035440 (2011).
[34] J. Quan, L. Linhart, M.-L. Lin, D. Lee, J. Zhu, C.-Y. Wang, W.-T. Hsu, J. Choi, J. Embley, C. Young, T. Taniguchi, K. Watanabe, C.-K. Shih, K. Lai, A. H. MacDonald, P.-H. Tan, F. Libisch, and X. Li, Nature Materials **20**, 1100 (2021).
[35] N. N. T. Nam and M. Koshino, Physical Review B **96** (2017), 10.1103/physrevb.96.075311.
[36] S. Carr, D. Massatt, S. B. Torrisi, P. Cazeaux, M. Luskin, and E. Kaxiras, Physical Review B **98** (2018), 10.1103/physrevb.98.224102.
[37] M. V. Berry and R. J. Mondragon, Proceedings of the Royal Society of London. A. Mathematical and Physical Sciences **412**, 53 (1987), https://royalsocietypublishing.org/doi/pdf/10.1098/rspa.1987.0080.
[38] C. Lanczos (1950).
[39] G. H. Golub and H. A. van der Vorst, Journal of Computational and Applied Mathematics **123**, 35 (2000), numerical Analysis 2000. Vol. III: Linear Algebra.
[40] R. Lehoucq, D. Sorensen, and C. Yang, "Arpack users' guide: Solution of large scale eigenvalue problems with implicitly restarted Arnoldi methods," (1997).
[41] I. Rungger and S. Sanvito, Phys. Rev. B **78**, 035407 (2008).
[42] R. Landauer, IBM Journal of Research and Development **1**, 223 (1957).
[43] M. Büttiker, Phys. Rev. B **38**, 9375 (1988).
[44] J. W. McClure, Phys. Rev. **104**, 666 (1956).
[45] J. Li, L. Lin, G.-Y. Huang, N. Kang, J. Zhang, H. Peng, Z. Liu, and H. Q. Xu, Journal of Applied Physics **123**, 064303 (2018), https://doi.org/10.1063/1.5009742.
[46] Y. Zhang, Y.-W. Tan, H. L. Stormer, and P. Kim, Nature **438**, 201 (2005).
[47] K. S. Novoselov, A. K. Geim, S. V. Morozov, D. Jiang, M. I. Katsnelson, I. V. Grigorieva, S. V. Dubonos, and A. A. Firsov, Nature **438**, 197 (2005).
[48] H. Nielsen and M. Ninomiya, Nuclear Physics B **185**, 20 (1981).
[49] D. J. Thouless, M. Kohmoto, M. P. Nightingale, and M. den Nijs, Phys. Rev. Lett. **49**, 405 (1982).

[50] F. Y ılmaz, F. N. Ünal, and M. O. Oktel, Phys. Rev. A **91**, 063628 (2015).

[51] F. Y ılmaz and M. O. Oktel, Phys. Rev. A **95**, 063628 (2017).

[52] Y. Cao, V. Fatemi, S. Fang, K. Watanabe, T. Taniguchi, E. Kaxiras, and P. Jarillo-Herrero, Nature **556**, 43 (2018).

[53] M. Yankowitz, S. Chen, H. Polshyn, Y. Zhang, K. Watanabe, T. Taniguchi, D. Graf, A. F. Young, and C. R. Dean, Science **363**, 1059 (2019), https://science.sciencemag.org/content/363/6431/1059.full.pdf.

[54] S. Möller, L. Banszerus, A. Knothe, C. Steiner, E. Icking, S. Trellenkamp, F. Lentz, K. Watanabe, T. Taniguchi, L. Glazman, V. Fal'ko, C. Volk, and C. Stampfer, "Probing two-electron multiplets in bilayer graphene quantum dots," (2021), arXiv:2106.08405.

[55] D. Moldovan, M. Anđelković, and F. Peeters, "pybinding v0.9.5: a Python package for tight- binding calculations," (2020), This work was supported by the Flemish Science Foundation (FWO-Vl) and the Methusalem Funding of the Flemish Government.

[56] J. Shi, J. Zhu, and A. H. MacDonald, Phys. Rev. B **103**, 075122 (2021).

[57] H. Kim, N. Leconte, B. L. Chittari, K. Watanabe, T. Taniguchi, A. H. MacDonald, J. Jung, and S. Jung, Nano Letters **18**, 7732 (2018).

[58] J. Jung, E. Laksono, A. M. DaSilva, A. H. MacDonald, M. Mucha-Kruczyński, and S. Adam, Phys. Rev. B **96**, 085442 (2017).

[59] B. Sachs, T. O. Wehling, M. I. Katsnelson, and A. I. Lichtenstein, Phys. Rev. B **84**, 195414 (2011).

[60] N. M. Freitag, T. Reisch, L. A. Chizhova, P. Nemes-Incze, C. Holl, C. R. Woods, R. V. Gorbachev, Y. Cao, A. K. Geim, K. S. Novoselov, and et al., Nature Nanotechnology **13**, 392 (2018).

[61] I. Souza, N. Marzari, and D. Vanderbilt, Phys. Rev. B **65**, 035109 (2001).

[62] N. Marzari and D. Vanderbilt, Phys. Rev. B **56**, 12847 (1997).

[63] C. R. Woods, L. Britnell, A. Eckmann, R. S. Ma, J. C. Lu, H. M. Guo, X. Lin, G. L. Yu, Y. Cao, R. Gorbachev, and et al., Nature Physics **10**, 451 (2014).

[64] K. V. Zakharchenko, M. I. Katsnelson, and A. Fasolino, Phys. Rev. Lett. **102**, 046808 (2009).

[65] S. Datta, *Electronic Transport in Mesoscopic Systems*, Cambridge Studies in Semiconductor Physics and Microelectronic Engineering (Cambridge University Press, 1997).

[66] S. Sanvito, C. Lambert, J. H. Jefferson, and A. Bratkovsky, Phys. Rev. B **59**, 11936 (1999).

[67] C. H. Lewenkopf and E. R. Mucciolo, Journal of Computational Electronics **12**, 203 (2013).